Imaging using Compressive Sensing Techniques for Planar Non-Destructive Testing at 60 GHz

Helander, Jakob; Ericsson, Andreas; Gustafsson, Mats; Martin, Torleif; Sjöberg, Daniel; Larsson, Christer

2017

CODEN:LUTEDX/(TEAT-7246)/1-17/(2017)

Imaging using Compressive Sensing Techniques for Planar Non-Destructive Testing at 60 GHz

Jakob Helander, Andreas Ericsson, Mats Gustafsson, Torleif Martin, Daniel Sjöberg, and Christer Larsson

Electromagnetic Theory
Department of Electrical and Information Technology
Lund University
Sweden

(TEAT-7246)/1-17/(2017): J. Helander, *etal*, Imaging using Compressive Sensing Techniques for Non-Destructive Testing

Jakob Helander
jakob.helander@eit.lth.se

Andreas Ericsson
jakob.helander@eit.lth.se

Mats Gustafsson
Mats.Gustafsson@eit.lth.se

†Torleif Martin
Torleif.Martin@eit.lth.se

Daniel Sjöberg
Daniel.Sjoberg@eit.lth.se

†Christer Larsson
Christer.Larsson@eit.lth.se

Department of Electrical and Information Technology
Electromagnetic Theory
Lund University
P.O. Box 118
SE-221 00 Lund
Sweden

† also at
Saab,
SE-581 88 Linköping,
Sweden

This is an author produced preprint version as part of a technical report series from the Electromagnetic Theory group at Lund University, Sweden. Homepage `http://www.eit.lth.se/teat`

Editor: Mats Gustafsson

Lund, February 16, 2017

Abstract

This paper presents imaging results from measurements of an industrial planar composite panel, utilizing two introduced algorithms for data post-processing. The system employs a planar near-field scanning set-up for characterizing defects in industrial planar composite panels in the 50–67 GHz band, and can be considered as a complementary diagnostic tool for non-destructive testing purposes. The introduced algorithms are based on the reconstruction of the illuminating source at the transmitter, enabling a separation of the sampled signal with respect to the location of its potential sources; the scatterers within the device under test or the transmitter respectively. The algorithm is extended to a L_1-minimization problem formulation exploiting the sparsity of the defects, which allows for compressive sensing techniques to be adapted for image retrieval. The algorithms are benchmarked against a more conventional imaging technique, based on the Fourier Transform, and it is seen that the complete imaging system provides increased dynamic range, improved resolution and reduced measurement time by removal of a reference measurement. Moreover, the system provides stable image quality over a range of frequencies.

1 Introduction

Non-destructive testing (NDT) is the science and practice of evaluating various properties of a device under test (DUT) without compromising its utility and usefulness [24]. Applications where NDT is used are for example: Welding inspection, structural evaluation of composite materials, medical imaging and security scanning [1, 24]. An alternative method that has attracted much attention in recent years is millimeter wave (mm-wave) NDT [1, 4, 16, 29]. The mm-wave spectrum is referring to the frequency range 30 – 300 GHz, corresponding to wavelengths of 1 – 10 mm.

In contrast to other methods, mm-wave NDT offers contactless testing of materials with nonionizing radiation and a high spatial resolution. Some applications where mm-wave NDT have been utilized are[29]: dielectric material characterization, detection of disbonds and delaminations in stratified composites, corrosion detection under paint, and near-field imaging applications such as security scanning [9] and medical screening [1]. Employing mm-wave NDT in near-field applications offers a number of advantageous properties. In general, these methods have the following properties: Low power, compact, robust, repeatable, relatively inexpensive, operator friendly and easily adaptable to existing industrial scanners [16].

Another strong point of mm-wave imaging systems is the inherent high spatial resolution, which relates to the short wavelength. Depending on the application, different frequencies of the mm-wave spectrum can be used, where higher frequencies imply a higher resolution but reduced penetration depth. The E-band (60 – 90 GHz, corresponding to wavelengths of 3.3 – 5 mm) provides a good compromise for NDT applications to detect flaws, material inhomogenities and inclusions in dielectrics [1], which is the main application of interest in this work.

A near-field mm-wave imaging system can either operate in reflection, such as in security applications [1, 9], or in transmission as in radome diagnostics [21] and near-

field antenna measurements [27]. The spatial sampling of the scattered signals can be acquired either through mechanical scanning [27] or electronic sampling by switching between spatially distributed transmit and receive antennas [1]. Depending on the application, either a single frequency or a broadband electromagnetic signal is used to illuminate the object. In this work, the focus is on transmission based near-field scanning systems. These systems traditionally utilize either planar, cylindrical or spherical scanning [10, 13, 27].

Once the signals of interest have been acquired over a given spatial area, using predefined sampling increments, the aim is to reconstruct the unknown sources on a given surface. This is an inverse problem which has traditionally been solved using reconstruction in the Fourier domain, commonly referred to in literature as time reversal, digital beam forming (DBF), aperture synthesis, back propagation, back projection or migration technique [25, 26].

An alternative is to utilize a minimization with respect to some norm. An image processing technique based on this theory that has gained a lot of interest is Compressive Sensing (CS). The most widely adopted CS methods address *sparse* and *linear* problems [5, 6, 14], where the strategy is to formulate the relation between the data and unknowns as a linear mapping, modeled by a rectangular matrix, and where the unknown vector has only a few non-zero entries. Consequently, the detection of small-scale defects and inhomogeneities, which in practice should result in few non-zero entries, are applications suitable for CS techniques. Furthermore, the theory behind CS states that, if adapted to a sparse problem, the sought after solution can be recovered using far fewer samples than what is classically required by the Nyquist theorem [17], allowing for a potentially reduced measurement time as the number of required data samples decreases.

The characteristics of CS have resulted in a fast development in a variety of applications related to electromagnetics [17] such as: array synthesis [19], antenna diagnostics [18], direction-of-arrival estimation [7], ground penetrating radar [11], and inverse scattering [20, 22, 23]. As spatial resolution, the achievable dynamic range and overall measurement time for acquiring data is generally considered the main measures of performance of an imaging system [1], the joint utilization of mm-wave NDT and CS offers a promising foundation for further development of near-field imaging systems.

The aim of this work is to find and characterize hidden defects in planar, composite panels of stratified dielectric media for an industrial application. By using a planar near-field scanning set-up, operating at 50 – 67 GHz, an imaging system is constructed that can be included as a complement to currently used diagnostic tools such as ultrasonic testing. A source separation algorithm is introduced that separates the components of the scattered signal related to the defects in the DUT from the total received signal by subtracting the illuminating field. This implies that no reference measurement is needed. After the illuminating field has been subtracted, a weak scattered field from a few sparse defects is acquired. This linear inverse problem is then well suited for CS. To this end, a CS algorithm has been implemented to find hidden sparse scatterers in a DUT.

The outline of the paper is as follows: The algorithms and their respective im-

plementations are presented in Sec. 2. In Sec. 3.1, the two algorithms are applied to synthetic data, and compared to the time reversal technique, in order to exclude any deterministic errors that might arise from a measurement when evaluating the performance of the algorithms. The complete imaging procedure is applied to data from measurements conducted on an industrial planar composite panel, manufactured at Saab Aerostructures (the Saab division for aircraft design and manufacturing) in Sec. 3.2. Finally, conclusions are presented in Sec. 4.

2 Algorithm Descriptions

For clarity, the notation used in the rest of this paper is summarized here: Bold face upper case and bold face lower case are used for matrix and vector notation respectively.

2.1 Measured Signal

The measured signal is sampled at a distance z from the illuminating antenna over a finite rectangular aperture. The sampling is performed over a uniform rectangular grid, and the measured signal for each fixed frequency in the corresponding grid point can be represented as the sampled signal s (a complex number at each spatial grid point):

$$\begin{aligned} &s(x_i, y_j, z) = s(x_1 + (i-1)\Delta, y_1 + (j-1)\Delta, z) \\ &i = 1, 2, \ldots, N_x \\ &j = 1, 2, \ldots, N_y. \end{aligned} \tag{1}$$

Here, Δ is the sample increment in the x- and y-direction, and (x_1, y_1) is the grid point in the lower left corner of the grid. The aggregated samples of the signal in the measurement plane (or if extracted, the samples of the field, see Sec. 2.2) for each fixed frequency is represented as a column vector with dimensions $N_\mathrm{m} \times 1$, where $N_\mathrm{m} = N_x N_y$.

2.2 Time Reversal Technique

For a measured signal $s(x, y, z_2)$ sampled continuously at a fixed distance $z = z_2$, the time reversal technique exploits the Fourier transform and its inverse in order to translate the signal between different xy-planes[26]. The signal's spatial spectrum at $z = z_2$ is

$$S(k_x, k_y, z_2) = \int_{-\infty}^{\infty} \int_{-\infty}^{\infty} s(x, y, z_2) \mathrm{e}^{\mathrm{j}(k_x x + k_y y)} \mathrm{d}x \mathrm{d}y, \tag{2}$$

where k_x and k_y are the x- and y-component of the wavenumber respectively. In the spectral domain, the signal can be translated to a xy-plane closer to the source using a simple exponential, i.e., the signal's spectrum at $z = z_1$ is:

$$S(k_x, k_y, z_1) = \mathrm{e}^{\mathrm{j}k_z d} S(k_x, k_y, z_2). \tag{3}$$

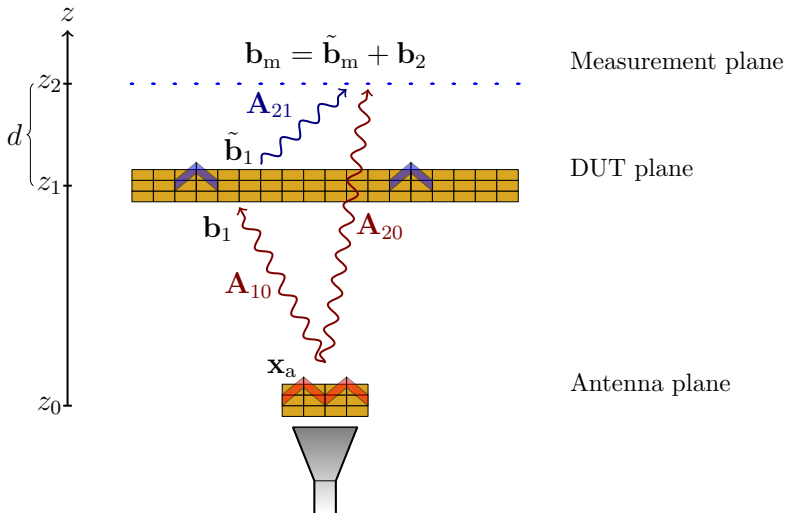

Figure 1: Single frequency algorithm scheme according to measurement set-up.

Here, $k_z = \sqrt{k^2 - k_x^2 - k_y^2}$, $d = z_1 - z_2 < 0$ and $k = 2\pi f/\mathrm{c}$ with f being the frequency and c being the speed of light in air. Applying the inverse Fourier transform yields the signal in the spatial domain: $s(x, y, z_1)$. For discrete signals, the usage of the discrete versions of the Fourier transform and its inverse allows for the time reversal technique to be efficiently implemented using Fast Fourier Transform (FFT) algorithms.

In order to retrieve the vector field components from the measured signal, it is necessary to compensate for the probe that samples the signal. The probe correction, explained in detail in [15, 27], is based on the a priori knowledge of the receiving characteristic of the probe. Using an open-ended waveguide, the far-field in the spectral domain can be modelled using formulas in [28]. The procedure can be used in order to extract either a scalar field or a vector field, where the vector field extraction requires the same signal to be measured twice. The two measurements can be obtained as the co-polarized and cross-polarized measurement respectively, by rotating the probe 90°.

The time reversal technique can be applied for image retrieval of a DUT containing defects, if an additional reference measurement is conducted and the field is normalized accordingly.

2.3 Source Separation Algorithm

A general model of the imaging set-up with appropriate field vectors and operators defined is seen in Fig. 1. As depicted in the figure, for a single frequency the field extracted from the corresponding discrete samples in the measurement plane is assembled into the $N_\mathrm{m} \times 1$ vector $\mathbf{b}_\mathrm{m}$. In order to expand the field in an arbitrary plane, all surfaces of interest are discretized into rectangular mesh cells with rooftop functions acting as local basis functions. The operator $\mathbf{A}_{ij}$ thus maps the currents in plane j to the field in plane i.

If the scattered field from the defects is small in amplitude compared to the total field in the measurement plane, then $\mathbf{b}_\mathrm{m}$ can be decomposed into the illuminating field $\mathbf{b}_2$ from the antenna and the slab of the DUT, and the scattered field $\tilde{\mathbf{b}}_\mathrm{m}$ arising only from the interior defects:

$$\mathbf{b}_\mathrm{m} = \tilde{\mathbf{b}}_\mathrm{m} + \mathbf{b}_2. \tag{4}$$

Using (4), $\tilde{\mathbf{b}}_\mathrm{m}$ can be extracted if $\mathbf{b}_2$ can be estimated appropriately. This is done by finding the currents on the antenna aperture represented by the $N_\mathrm{a} \times 1$ vector $\mathbf{x}_\mathrm{a}$, using the operator $\mathbf{A}_{20}$ (size $N_\mathrm{m} \times N_\mathrm{a}$). A singular value decomposition (SVD) is applied to $\mathbf{A}_{20}$:

$$\mathbf{A}_{20} = \mathbf{U}\boldsymbol{\Sigma}\mathbf{V}^\mathrm{H}. \tag{5}$$

Here, $\mathbf{U}$ and $\mathbf{V}$ are unitary matrices of size $N_\mathrm{m} \times N_\mathrm{m}$ and $N_\mathrm{a} \times N_\mathrm{a}$ respectively, and $\boldsymbol{\Sigma}$ is a diagonal matrix of size $N_\mathrm{m} \times N_\mathrm{a}$ containing N_a non-zero positive singular values σ_n $(n = 1, 2, \ldots, N_\mathrm{a})$ of $\mathbf{A}_{20}$. The normalized singular values are truncated according to a prescribed threshold τ, and the pseudo inverse is constructed[8]:

$$\mathbf{A}_{20}^\dagger = \mathbf{V}\boldsymbol{\Sigma}^\dagger\mathbf{U}^\mathrm{H}. \tag{6}$$

Here, $\boldsymbol{\Sigma}^\dagger$ is a diagonal matrix, with all entries corresponding to singular values whose normalized value is below τ set to zero. The remaining entries contain the reciprocal of the corresponding singular value itself. Applying $\mathbf{A}_{20}^\dagger$ to the measured field $\mathbf{b}_\mathrm{m}$ yields

$$\mathbf{x}_\mathrm{a} = \mathbf{A}_{20}^\dagger \mathbf{b}_\mathrm{m}, \tag{7}$$

and the field contribution from the antenna, $\mathbf{b}_2$, is found as:

$$\mathbf{b}_2 = \mathbf{A}_{20}\mathbf{x}_\mathrm{a}. \tag{8}$$

After finding $\mathbf{b}_2$, the analysis is restricted to the scattered field $\tilde{\mathbf{b}}_\mathrm{m}$, where the source separation algorithm utilizes the time reversal technique to retrieve the final image in the DUT plane. The CS algorithm introduced in the upcoming section, is instead based on the formulation of the L_1-minimization optimization problem. The partitioning of the field as a result of the source separation is illustrated in Fig. 2.

2.4 Compressive Sensing Algorithm

The CS algorithm utilizes the SPGL1 Matlab solver based on the general basis pursuit denoise (BPDN) L_1-minimization problem [2, 3]. For a single frequency, the target image can be acquired from the scattered field $\tilde{\mathbf{b}}_\mathrm{m}$, by finding the corresponding scattered field $\tilde{\mathbf{b}}_1$ in the DUT plane. The initial optimization problem is then formulated as:

$$\begin{aligned} &\text{minimize} && ||\tilde{\mathbf{b}}_1||_1 \\ &\text{subject to} && ||\mathbf{A}_{21}\tilde{\mathbf{b}}_1 - \tilde{\mathbf{b}}_\mathrm{m}||_2 \leq \sigma, \end{aligned} \tag{9}$$

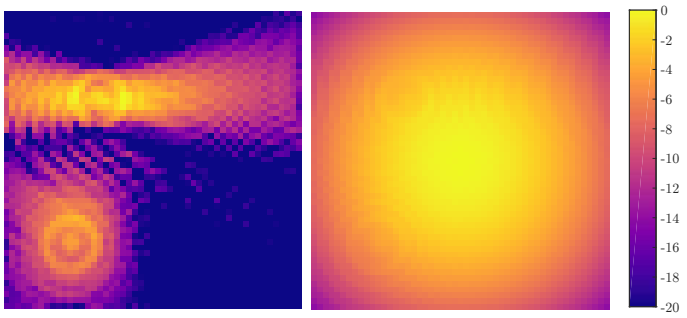

Figure 2: Extracted scattered field $\tilde{\mathbf{b}}_\mathrm{m}$ (left) from a total field $\mathbf{b}_\mathrm{m}$ in the measurement plane (right) from an example simulation using the theory presented in Sec. 2.3. The figures depict independently normalized absolute values of the fields in dB-scale. The relative power difference between total and scattered field is $\simeq 30\,\mathrm{dB}$.

where σ is a user-defined threshold. In order to reconstruct properties of the defects rather than the scattered field $\tilde{\mathbf{b}}_1$, we introduce the scattering amplitudes $\mathbf{s}$ as

$$\tilde{\mathbf{b}}_1 = \mathbf{B}_1 \mathbf{s}, \tag{10}$$

with

$$\mathbf{B}_1 = \mathrm{diag}(\mathbf{b}_1) = \begin{bmatrix} b_{1,1} & 0 & \dots & 0 \\ 0 & b_{1,2} & \dots & 0 \\ \vdots & \vdots & \ddots & \vdots \\ 0 & 0 & \dots & b_{1,N_1} \end{bmatrix}$$

representing the incident field on the panel at $z = z_1$ from the antenna, see Fig. 1. N_1 spatial grid points are assumed in the DUT plane. By defining the appropriate operator $\mathbf{A}_{10}$ (dimensions $N_1 \times N_\mathrm{a}$), $\mathbf{b}_1$ can be found through

$$\mathbf{b}_1 = \mathbf{A}_{10} \mathbf{x}_\mathrm{a}, \tag{11}$$

using $\mathbf{x}_\mathrm{a}$ from (7). The scattering amplitudes $\mathbf{s}$ now comprises N_1 unknowns, induced by the scatterers in the DUT plane. In the scenario where only small defects exist, $\mathbf{s}$ should be a vector containing only few non-zero elements representing these defects (or rather, the area of the defects). The optimization problem can then be formulated as:

$$\begin{aligned} &\text{minimize} && ||\mathbf{s}||_1 \\ &\text{subject to} && ||\mathbf{A}_{21}\mathbf{B}_1\mathbf{s} - \tilde{\mathbf{b}}_\mathrm{m}||_2 \leq \sigma. \end{aligned} \tag{12}$$

Furthermore, the illuminating source does not distribute the power uniformly over any arbitrary xy-plane (DUT or measurement). Since (12) weights the scattering amplitudes with the incident field in the DUT plane, $\mathbf{B}_1$, the whole formulation is multiplied with the magnitude of the inverse of the incident field in the measurement plane, $\mathbf{B}_{2,\mathrm{inv}}$, accordingly:

$$\begin{aligned} &\text{minimize} && ||\mathbf{s}||_1 \\ &\text{subject to} && ||\mathbf{B}_{2,\mathrm{inv}}\mathbf{A}_{21}\mathbf{B}_1\mathbf{s} - \mathbf{B}_{2,\mathrm{inv}}\tilde{\mathbf{b}}_\mathrm{m}||_2 \leq \sigma. \end{aligned} \tag{13}$$

Here, $\mathbf{B}_{2,\text{inv}}$ is defined as:

$$\mathbf{B}_{2,\text{inv}} = \begin{bmatrix} |b_{2,1}|^{-1} & 0 & \dots & 0 \\ 0 & |b_{2,2}|^{-1} & \dots & 0 \\ \vdots & \vdots & \ddots & \vdots \\ 0 & 0 & \dots & |b_{2,N_\text{m}}|^{-1} \end{bmatrix}.$$

The threshold σ is chosen accordingly: For a known field $\tilde{\mathbf{b}}_\text{m}$, an estimate of the scattering amplitudes $\hat{\mathbf{s}}$ is retrieved by time reversing $\mathbf{A}_{21}$ using its conjugate $\mathbf{A}_{21}^*$:

$$\mathbf{B}_1\hat{\mathbf{s}} = \mathbf{A}_{21}^*\tilde{\mathbf{b}}_\text{m}. \tag{14}$$

By applying $\mathbf{A}_{21}$ to $\mathbf{B}_1\hat{\mathbf{s}}$, the estimated scattered field in the measurement plane $\hat{\mathbf{b}}_\text{m}$ is found as:

$$\hat{\mathbf{b}}_\text{m} = \mathbf{A}_{21}\mathbf{B}_1\hat{\mathbf{s}} = \mathbf{A}_{21}\mathbf{A}_{21}^*\tilde{\mathbf{b}}_\text{m}. \tag{15}$$

Finally, σ is chosen as the L_2-norm of the difference between the initial scattered field $\tilde{\mathbf{b}}_\text{m}$ and its estimate $\hat{\mathbf{b}}_\text{m}$:

$$\sigma = ||\tilde{\mathbf{b}}_\text{m} - \hat{\mathbf{b}}_\text{m}||_2 = ||(1 - \mathbf{A}_{21}\mathbf{A}_{21}^*)\tilde{\mathbf{b}}_\text{m}||_2. \tag{16}$$

Comment on implementation

Given that the measurement and DUT plane are discretized identically, it follows that $\mathbf{A}_{21}$ is a block Toeplitz matrix. Due to the large number of grid points necessary for a reasonable resolution, it is not desirable to compute the complete matrix operator, which would severely impact the computational efficiency of the algorithm. Rather, $\mathbf{A}_{21}$ can be extended to a circulant matrix due to its Toeplitz characteristic, and the general linear operations $\mathbf{A}_{21}\mathbf{x}$ and $\mathbf{A}_{21}^*\mathbf{b}$ (for suitably chosen vectors $\mathbf{x}$ and $\mathbf{b}$) can instead be evaluated efficiently in a matrix free way using an FFT algorithm[8, 12].

3 Performance

The three implemented algorithms are:

1. The time reversal technique, as described in Sec. 2.2. This technique employs time reversal of the field $\mathbf{b}_\text{m}$ in the measurement plane with DUT present and a free space reference. The final image is obtained after normalization with the free space field back-propagated to the DUT plane.

2. The source separation algorithm. This algorithm utilizes source separation to estimate the scattered field $\tilde{\mathbf{b}}_\text{m}$ in the measurement plane (Sec. 2.3), and thereafter employs time reversal of $\tilde{\mathbf{b}}_\text{m}$ (Sec. 2.2) in order to retrieve the final image.

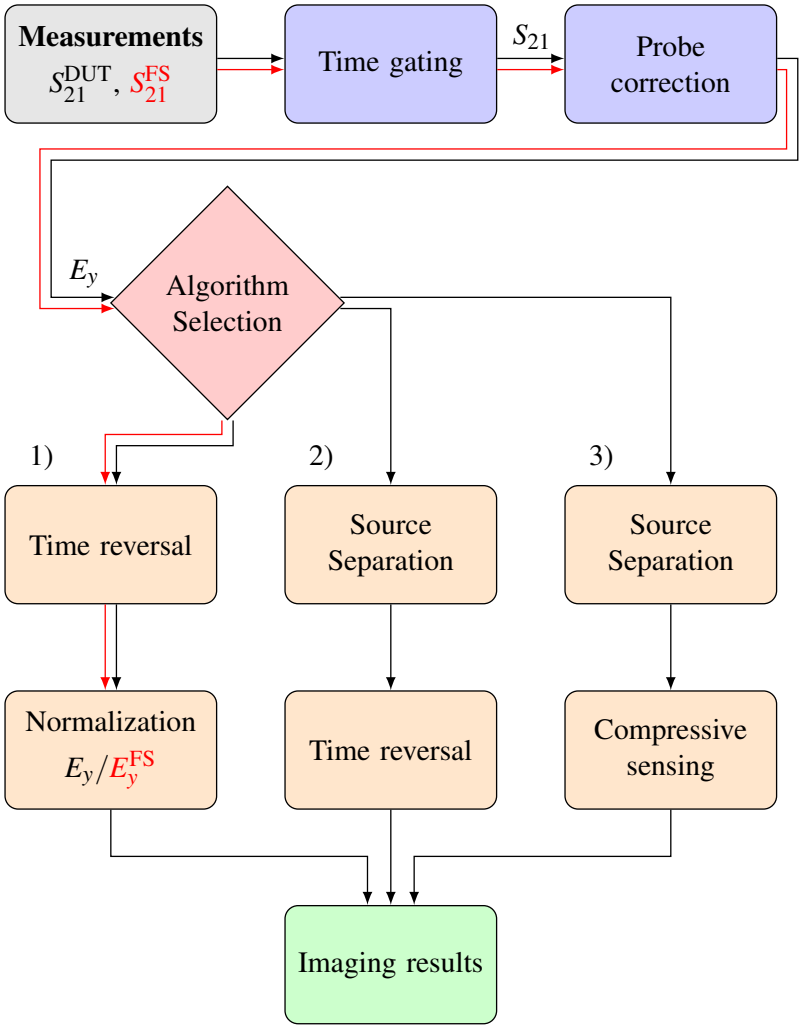

Figure 3: Block diagram depicting the post processing steps used in this work. The top row corresponds to processing that were carried out for all measurement data. The three parallel schemes at the bottom correspond to 1) the time reversal technique, 2) the source separation algorithm and 3) the CS algorithm.

3. The CS algorithm. This algorithm utilizes source separation to estimate the scattered field $\tilde{\mathbf{b}}_{\mathrm{m}}$ in the measurement plane (Sec. 2.3), and thereafter employs the general BPDN L_1-minimization optimization problem formulation in (13), in order to retrieve the final image (Sec. 2.4).

A block diagram describing the algorithms can be seen in Fig. 3. As depicted, the top row of blocks represents measurement post-processing procedures and thus only apply to measured data (Sec. 3.2). When executing the time reversal routine in algorithm 1) or 2), interpolation of the data can be employed using zero padding of the signal's spatial spectrum. For all results presented in this section, sampling is carried out in the measurement plane at $z_2 = 530\,\mathrm{mm}$, with $\Delta = 5\,\mathrm{mm}$ and $N_{\mathrm{m}} = 51 \times 51 = 2\,601$, resulting in a total finite square aperture of $250 \times 250\,\mathrm{mm}^2$. The DUT plane is at $z_1 = 470\,\mathrm{mm}$ with $N_1 = 203 \times 203 = 41\,209$ number of

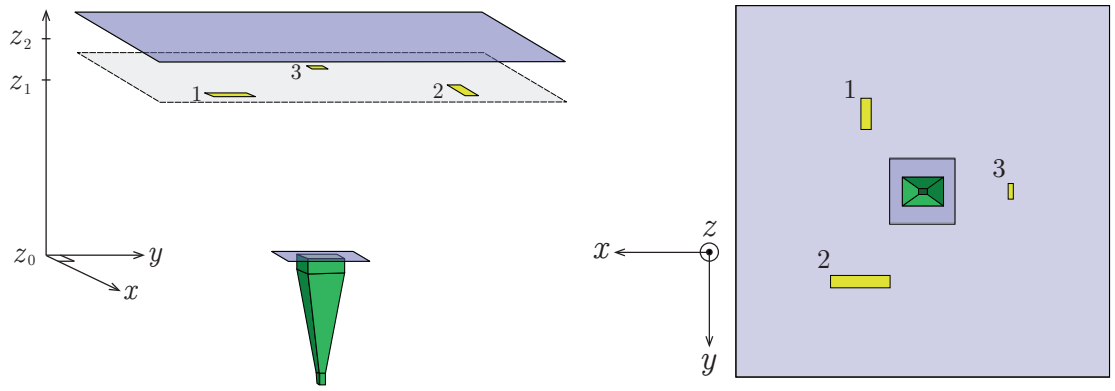

(a) Side view. (b) Top view.

Figure 4: Simulation set-up in FEKO for synthetic data generation. Measures not to scale. Highlighted regions in (a) denote the measurement-, DUT- and antenna plane respectively in descending order.

spatial grid points. The distance between the measurement plane and the DUT plane then becomes $d = 60\,\text{mm}$. The antenna aperture plane is at $z_0 = 0\,\text{mm}$. Note that in the frequency band of interest $50 - 67\,\text{GHz}$, the sample increment is $\Delta \approx \lambda$ and thereby the Nyquist criterion is violated. However, no aliasing is introduced that affects the final image due to the fact that the geometrical set-up limits the possible incident plane waves under consideration, or equivalently restricts the (k_x, k_y)-spectrum. Consequently, any aliasing that occurs falls outside of the wavenumber region of interest.

3.1 Synthetic Data

In this section the above described algorithms are employed on synthetic data, extracted from simulations using FEKO. This discards any deterministic measurement errors that might appear when measured data is considered, and consequently provides a proof of concept of the algorithms themselves.

The E_y-component (co-polarization) in the aperture of a standard gain horn antenna at $60\,\text{GHz}$ is used as the illuminating source ($z_0 = 0\,\text{mm}$), and three rectangular resistive sheets with $R = 100\,\Omega$ are placed at $z_1 = 470\,\text{mm}$ representing the DUT. The set-up can be seen in Fig. 4. With labelling according to Fig. 4b, the dimensions of the resistive sheets are $1.5 \times 10\,\text{mm}^2$, $5 \times 2.5\,\text{mm}^2$ and $1 \times 1\,\text{mm}^2$.

Retrieved images using the time reversal technique, source separation algorithm and the CS algorithm can be seen in Fig. 5. As seen, for the depicted color range ($[-60, 0]\,\text{dB}$), the CS algorithm provides the best dynamic range as only scattering amplitudes related to the physical dimension of the resistive sheets have non-zero entries, i.e., the sparse solution to the problem is found. The time reversal technique gives little information whereas the source separation algorithm manages to detect the defects, with noticeable low power noise present. Due to the large difference in dynamic range for the different algorithms, the images from the time reversal

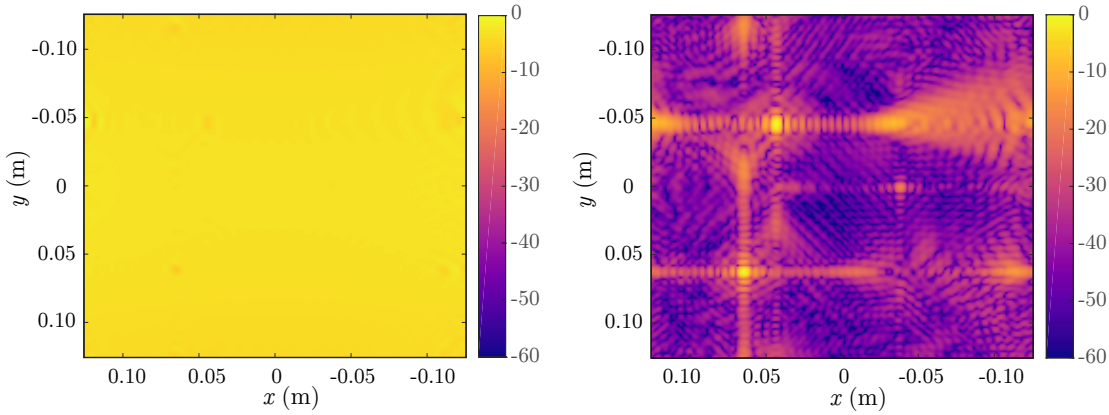

(a) Time reversal technique.

(b) Source separation algorithm.

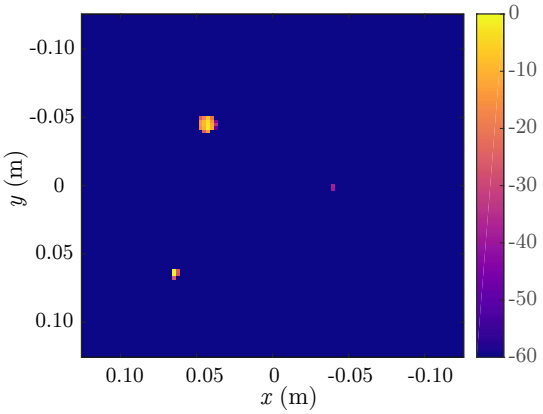

(c) CS algorithm.

Figure 5: Retrieved images at 60 GHz for the synthetic data using the three different algorithms. (a) depicts $|\mathrm{E}_y|/|\mathrm{E}_y^{\mathrm{FS}}|$, were $\mathrm{E}_y^{\mathrm{FS}}$ denotes the free space reference measurement, (b) depicts $|\mathrm{E}_y|$, and (c) depicts the absolute value of the scattering amplitudes $\mathbf{s}$. All figures are in normalized dB-scale ($20\log_{10}(|u|/\max(|u|))$, where u is the parameter being plotted) with color range $[-60,\, 0]$ dB.

technique and source separation algorithm are shown in Fig. 6 for customized color ranges. It is seen that the source separation algorithm provides a dynamic range of around $\simeq 20$ dB. As Fig. 5 and 6 (a) depict the time reversed field normalized with a free space measurement ($|\mathrm{E}_y|/|\mathrm{E}_y^{\mathrm{FS}}|$), the shadowing effect from the resistive sheets is clearly seen as the amplitude around the defects is lower than the surrounding medium. However, both the source separation algorithm and CS algorithm act on the scattered field using (4), and consequently the images in Fig. 5 (b), (c) and Fig. 6 (b) show the resistive sheets as the maximum amplitude in the DUT plane. Truncation effects, i.e. sidelobes, arising from the finite aperture of the measurement plane can be seen for both the time reversal technique and source separation algorithm, most clearly seen in Fig. 5 (b) as the vertical- and horizontal lines springing from the resistive sheets. The sidelobes can be suppressed by applying an appropriate windowing function, reducing the effect of the finite aperture of the

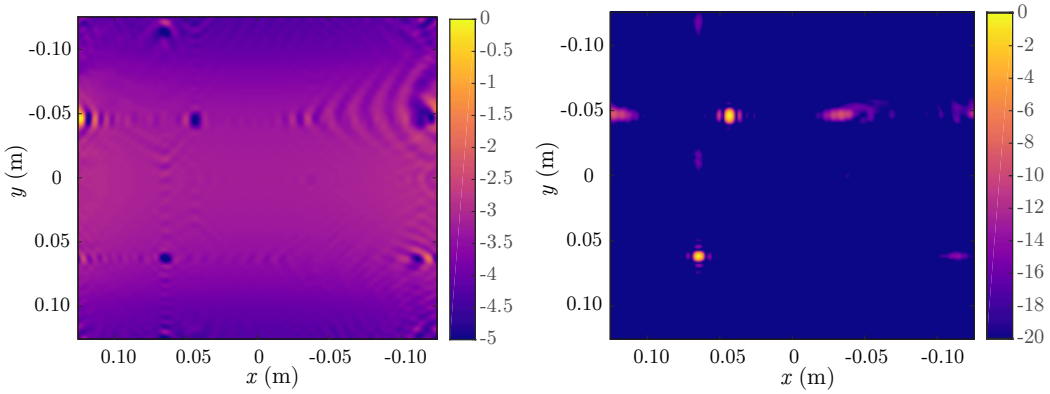

(a) Time reversal technique.

(b) Source separation algorithm.

Figure 6: Retrieved images at 60 GHz for the synthetic data using the time reversal technique and source separation algorithm with customized color range. (a) depicts $|\mathrm{E}_y|/|\mathrm{E}_y^{\mathrm{FS}}|$ were $|\mathrm{E}_y^{\mathrm{FS}}|$ denotes the free space reference measurement, and (b) depicts $|\mathrm{E}_y|$. Both figures are in normalized dB-scale ($20\log_{10}(|u|/\max(|u|))$, where u is the parameter being plotted) with color range: (a) $[-5, 0]$ dB, and (b) $[-20, 0]$ dB.

measurement plane, with the cost of degraded resolution. However, these sidelobes do not appear for the CS algorithm, due to the usage of operators for transforming between xy-planes. Moreover, the CS algorithm manages to resolve the $1 \times 1\,\mathrm{mm}^2$ ($0.2\lambda \times 0.2\lambda$) defect, whereas this defect is not detected by neither the time reversal technique nor the source separation algorithm.

3.2 Measurements

Measurements were carried out in the institutional laboratory at Lund University, Sweden. The illuminating source was chosen as a 50 – 67 GHz standard gain horn antenna, and an open-ended waveguide was used as the scanning probe. A single planar scan was conducted, with both horn and probe being y-polarized. The transmitted signal was measured using an Agilent E8361A network analyzer, and a low noise amplifier (LNA) was added on the receiver side. The transmit power was -7 dBm, the intermediate frequency (IF) bandwidth was set to 300 Hz and a linearly spaced frequency sampling with 201 points across the whole operational band of the horn antenna was used.

In order to acquire the necessary data as input for the algorithms, post-processing routines were employed on the measured S_{21}, as seen in the top row of blocks in Fig. 3. First, multipath scattering components of the signal are suppressed by applying an appropriate window function in the time domain, here chosen as a Hanning window. An interesting remark is that even with a free space path loss of $\simeq 68\,\mathrm{dB/m}$ at 60 GHz, and additional losses due to reflection and surrounding absorbers, the data filtering resulted in a considerable improvement of the purity of the S_{21} over the measurement aperture. Secondly, probe correction is applied in order to extract the field components from the S_{21} as described in Sec. 2.2. Using

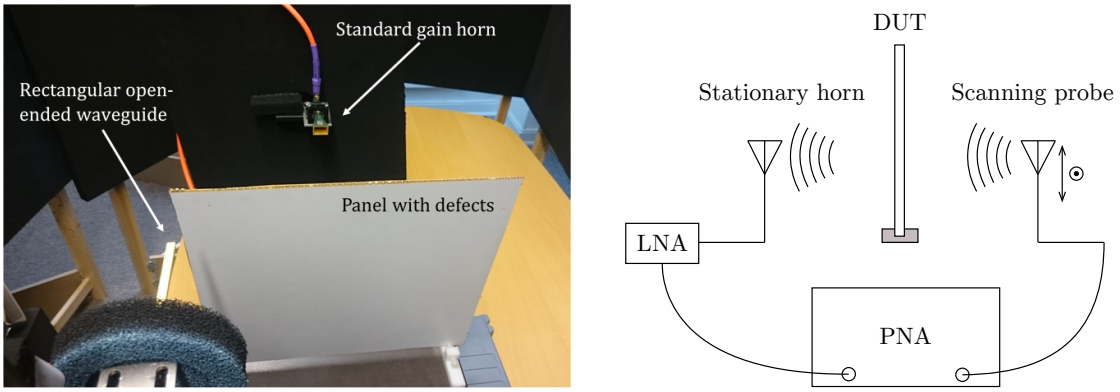

(a) (b)

Figure 7: Photo (a), and block schematic (b) of the measurement set-up. Receiving antenna is a 50 – 67 GHz standard gain horn antenna, and the transmitting scanning probe is a rectangular open-ended waveguide. Surrounding absorbers are seen in black (a).

one planar scan, only a single scalar component may be extracted, here chosen as the co-polarized component of the electric field, i.e., E_y according to the alignment of the horn and the probe. It should be noted that the probe correction is not limited to a specific field or component [15]. Rather, there exists a flexibility in which field and which component to extract. As mentioned in Sec. 2.2, an additional planar scan with the probe rotated 90° would allow for the extraction of the complete vector fields, with the cost of doubling the total measurement time.

The measurement set-up is shown in Fig. 7. The DUT is an industrial planar composite panel provided by Saab Aerostructures. The panel consists of a 2 mm thick low permittivity over-expanded Nomex honeycomb core, sandwiched between two 0.5 mm sheets of cyanate ester and quartz fabric. Defects were inserted into the Nomex honeycomb core, and the panel was assembled using a cyanate ester adhesive film and covered with a fluoropolymer film. The full dimension of the DUT is $300 \times 300 \times 3\,\text{mm}^3$. A picture of the inner layers of the panel before assembly is seen in Fig. 10. Defects in the right column are metallic while the remaining defects are dielectric. The largest dimension of all defects are between $2 - 20$ mm, i.e. ranging in size from sub-wavelength to a few wavelengths of the illuminating signal. With the geometrical settings presented earlier, one planar scan took 4 h to conduct, i.e., the total measurement time for retrieving the necessary data for the different algorithms is 8 h, 4 h and 4 h for the time reversal technique, the source separation algorithm and the CS algorithm respectively.

Retrieved images using the time reversal technique, the source separation algorithm and the CS algorithm can be seen in Fig. 8 at $f = 60$ GHz. Note the customized color scale for every image, motivated by the large difference in dynamic range achieved by the different algorithms. The image quality obtained in the synthetic case is maintained for the measured data. As for the synthetic case, the CS algorithm provides the best dynamic range. The source separation algorithm and

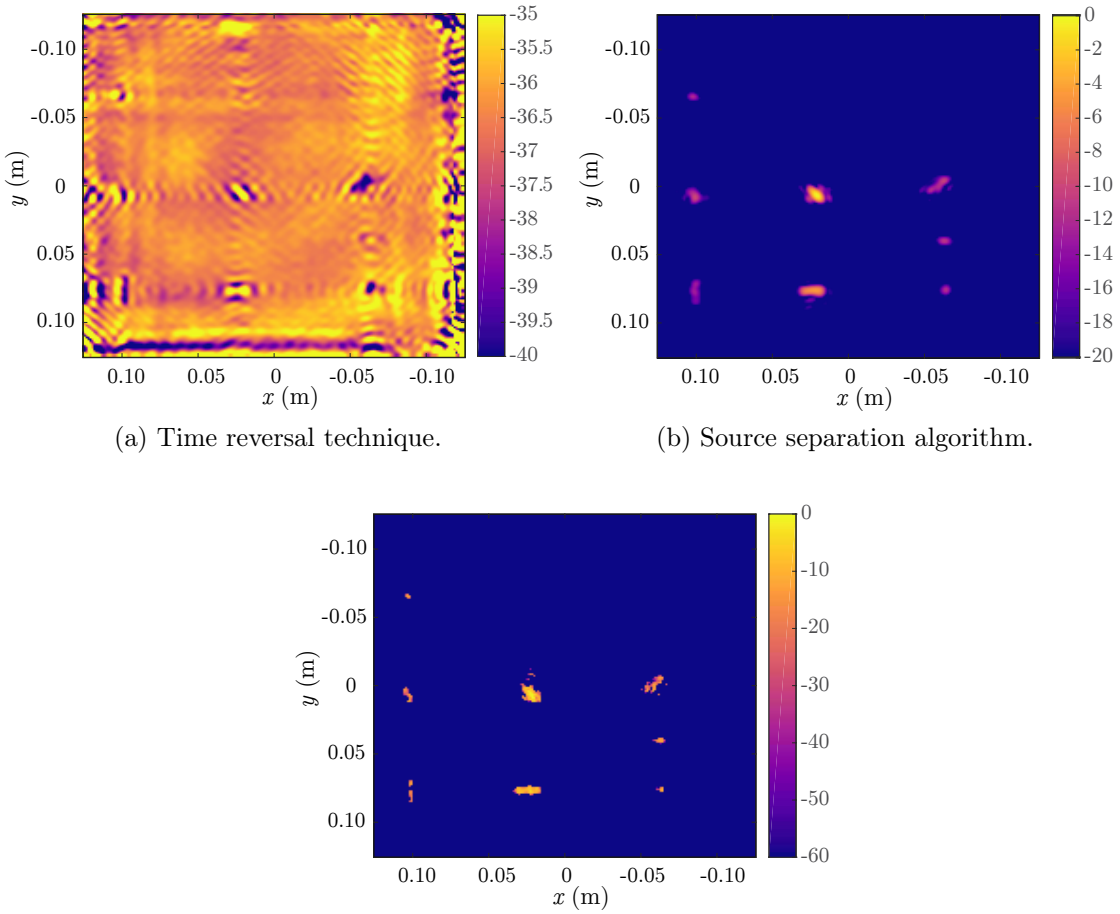

(a) Time reversal technique.

(b) Source separation algorithm.

(c) CS algorithm.

Figure 8: Retrieved images at 60 GHz for the measured data using the three different algorithms. (a) depicts $|\mathrm{E}_y|/|\mathrm{E}_y^{\mathrm{FS}}|$, were $\mathrm{E}_y^{\mathrm{FS}}$ denotes the free space reference measurement, (b) depicts $|\mathrm{E}_y|$, and (c) depicts the absolute value of the scattering amplitudes $\mathbf{s}$. All figures are in normalized dB-scale ($20\log_{10}(|u|/\max(|u|))$, where u is the parameter being plotted) with color range: (a) $[-40,\ \text{-}35]$ dB, (b) $[-20,\ 0]$ dB and (c) $[-60,\ 0]$ dB.

CS algorithm provide stable images regardless of the choice of frequency, demonstrated by the similarity of the equivalent images at $f = 61$ GHz shown in Fig. 9 (b) and (c). Errors arising from the measurement set-up can be seen to affect the image quality of Fig. 8 and 9 (a) to a larger extent, perhaps explained by the exploitation of data from two independent measurements (one with DUT present and one free space reference). Whereas the dynamic range is maintained, the color scale is different for the different frequencies in (a) in order to provide the best image. The effect of the weighting compensation introduced by the operator $\mathbf{B}_{2,\mathrm{inv}}$ can also be seen in Fig. 8 and 9 (c), as the scattering amplitudes for all defects are of the same magnitude unlike as in (a) and (b).

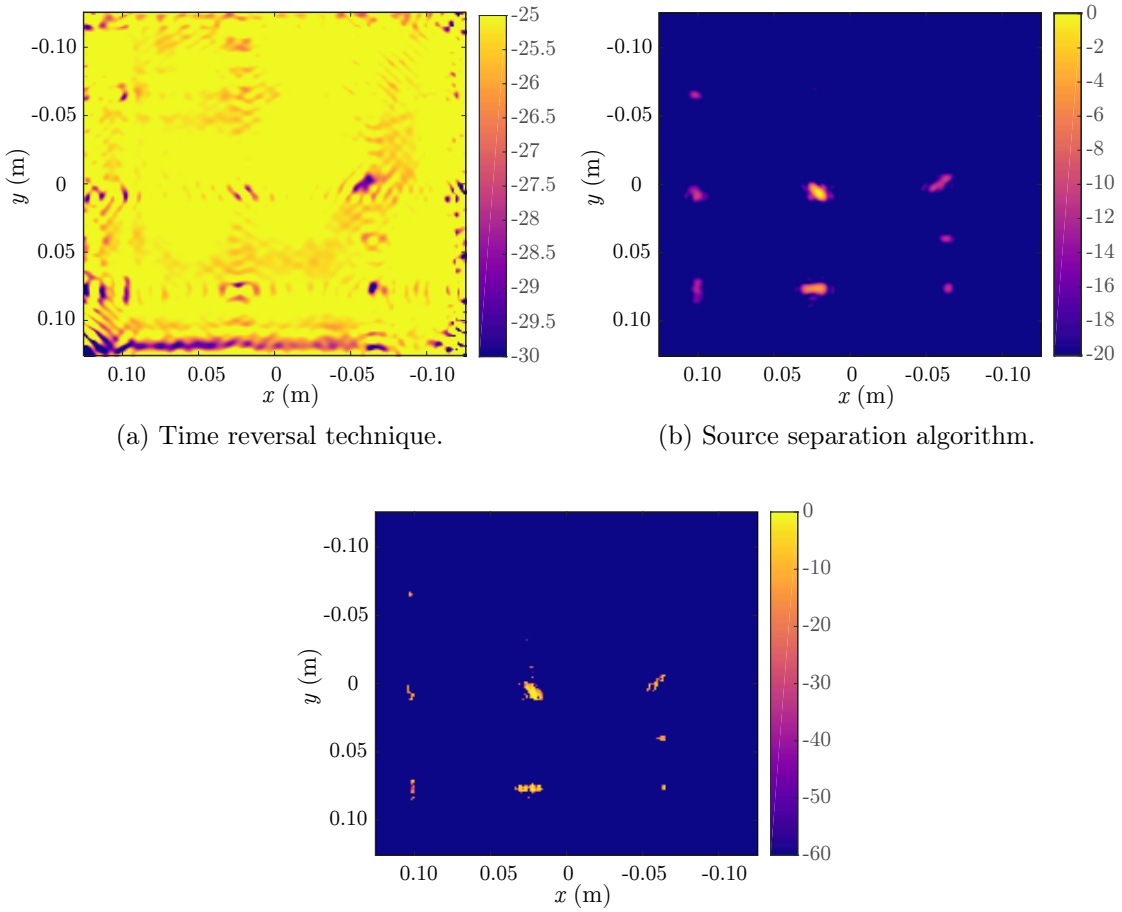

(a) Time reversal technique.

(b) Source separation algorithm.

(c) CS algorithm.

Figure 9: Retrieved images at 61 GHz for the measured data using the three different algorithms. (a) depicts $|\mathrm{E}_y|/|\mathrm{E}_y^{\mathrm{FS}}|$, were $\mathrm{E}_y^{\mathrm{FS}}$ denotes the free space reference measurement, (b) depicts $|\mathrm{E}_y|$, and (c) depicts the absolute value of the scattering amplitudes $\mathbf{s}$. All figures are in normalized dB-scale ($20\log_{10}(|u|/\max(|u|))$, where u is the parameter being plotted) with color range: (a) $[-30,\ -25]$ dB, (b) $[-20,\ 0]$ dB and (c) $[-60,\ 0]$ dB.

4 Conclusion

A complete imaging system using a planar near-field scanning set-up operating in the 50 – 67 GHz band has been presented. Its potential as a complementary tool for industrial NDT diagnostic purposes has been validated through measurements on an industrial planar composite panel using two introduced post-processing algorithms. The source separation algorithm can be regarded as a stepping-stone in the development of the more efficient CS algorithm, yet both algorithms provide noticeable enhancements compared to the more conventional time reversal technique. These enhancements include reduction of measurement time by removal of a reference measurement, increased dynamic range, and stable image quality over a range of frequencies; all are critical measures for system performance.

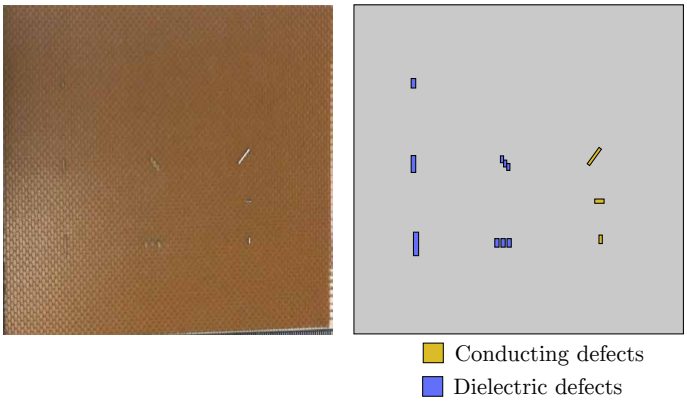

Figure 10: Photo (left) and schematic (right) of the panel under test as seen from the probe. The size of the panel is $300 \times 300 \times 3\,\mathrm{mm}^3$.

Further development of the CS algorithm is ongoing, mainly for reduction of measurement time while maintaining image quality. The single frequency problem formulation provided in (13) allows for a straightforward extension to the multiple frequency scenario, in which data from several fixed frequencies can be utilized in order to solve for the scattering amplitudes. Potentially, this would allow for a reduction in spatial samples without compromising image quality. This implementation is currently in progress.

Acknowledgements

The work presented is financed by the Swedish Armed Forces, the Swedish Defence Materiel Ad- ministration, the Swedish Governmental Agency for Innovation Systems, and Swedish Foundation for Strategic Research.

The authors would like to thank Mikael Petersson at Saab Aerostructures for manufacturing the test panel. The authors would also like to thank Carl Gustafsson and Iman Vakili for assisting with the measurements.

References

[1] S. S. Ahmed, A. Schiessl, F. Gumbmann, M. Tiebout, S. Methfessel, and L.-P. Schmidt. “Advanced microwave imaging”. *IEEE microwave magazine* 13 (6) (2012): pp. 26–43.

[2] E. van den Berg and M. P. Friedlander. “Probing the Pareto frontier for basis pursuit solutions”. *SIAM Journal on Scientific Computing* 31 (2) (2008): pp. 890–912.

[3] E. van den Berg and M. P. Friedlander. *SPGL1: A solver for large-scale sparse reconstruction*. 2007.

[4] J. Blitz. "Electrical and Magnetic Methods of Non-Destructive Testing". Vol. 3. Springer Science & Business Media, 2012.

[5] E. Candes and J. Romberg. "Sparsity and incoherence in compressive sampling". *Inverse problems* 23 (3) (2007): p. 969.

[6] E. J. Candès and M. B. Wakin. "An introduction to compressive sampling". *IEEE signal processing magazine* 25 (2) (2008): pp. 21–30.

[7] M. Carlin, P. Rocca, G. Oliveri, F. Viani, and A. Massa. "Directions-of-arrival estimation through Bayesian compressive sensing strategies". *IEEE Transactions on Antennas and Propagation* 61 (7) (2013): pp. 3828–3838.

[8] G. H. Golub and C. F. van Loan. "Matrix Computations". The Johns Hopkins University Press, 1983.

[9] B. Gonzalez-Valdes, Y. Alvarez, S. Mantzavinos, C. M. Rappaport, F. Las-Heras, and J. Á. Martínez-Lorenzo. "Improving security screening: a comparison of multistatic radar configurations for human body imaging". *IEEE Antennas and Propagation Magazine* 58 (4) (2016): pp. 35–47.

[10] S. Gregson, J. McCormick, and C. Parini. "Principles of planar near-field antenna measurements". Vol. 53. IET, 2007.

[11] A. C. Gurbuz, J. H. McClellan, and W. R. Scott. "A compressive sensing data acquisition and imaging method for stepped frequency GPRS". *IEEE Transactions on Signal Processing* 57 (7) (2009): pp. 2640–2650.

[12] M. Gustafsson, M. Sebesta, B. Bengtsson, S.-G. Pettersson, P. Egelberg, and T. Lenart. "High resolution digital transmission microscopy—a Fourier holography approach". *Optics and Lasers in Engineering* 41 (3) (2004): pp. 553–563.

[13] J. E. Hansen, ed. "Spherical Near-Field Antenna Measurements". IEE electromagnetic waves series 26. Peter Peregrinus Ltd., 1988.

[14] S. Ji, Y. Xue, and L. Carin. "Bayesian compressive sensing". *IEEE Transactions on Signal Processing* 56 (6) (2008): pp. 2346–2356.

[15] D. Kerns. "Correction of near-field antenna measurements made with an arbitrary but known measuring antenna". *Electron. Lett.* 6 (11) (1970): pp. 346–347.

[16] S. Kharkovsky and R. Zoughi. "Microwave and millimeter wave nondestructive testing and evaluation - overview and recent advances". *IEEE Instrumentation & Measurement Magazine* 10 (2) (2007): pp. 26–38.

[17] A. Massa, P. Rocca, and G. Oliveri. "Compressive sensing in electromagnetics-a review". *IEEE Antennas Propag. Mag.* 57 (1) (2015): pp. 224–238.

[18] M. D. Migliore. "A compressed sensing approach for array diagnosis from a small set of near-field measurements". *IEEE Transactions on Antennas and Propagation* 59 (6) (2011): pp. 2127–2133.

[19] G. Oliveri and A. Massa. "Bayesian compressive sampling for pattern synthesis with maximally sparse non-uniform linear arrays". *IEEE Transactions on Antennas and Propagation* 59 (2) (2011): pp. 467–481.

[20] L. Pan, X. Chen, and S. P. Yeo. "A compressive-sensing-based phaseless imaging method for point-like dielectric objects". *IEEE Transactions on Antennas and Propagation* 60 (11) (2012): p. 5472.

[21] K. Persson, M. Gustafsson, G. Kristensson, and B. Widenberg. "Radome diagnostics — source reconstruction of phase objects with an equivalent currents approach". *IEEE Trans. Antennas Propag.* 62 (4) (2014).

[22] L. Poli, G. Oliveri, P. P. Ding, T. Moriyama, and A. Massa. "Multifrequency Bayesian compressive sensing methods for microwave imaging". *JOSA A* 31 (11) (2014): pp. 2415–2428.

[23] L. C. Potter, E. Ertin, J. T. Parker, and M. Cetin. "Sparsity and compressed sensing in radar imaging". *Proc. IEEE* 98 (6) (2010): pp. 1006–1020.

[24] P. J. Shull. "Nondestructive Evaluation: Theory, Techniques, and Applications". New York: Marcel Dekker, 2002.

[25] M. Soumekh. "Fourier array imaging". Prentice-Hall, Inc., 1994.

[26] R. H. Stolt. "Migration by fourier transform". *Geophysics* 43 (1) (1978): pp. 23–48.

[27] A. D. Yaghjian. "An overview of near-field antenna measurements". *IEEE Trans. Antennas Propag.* 34 (1) (1986): pp. 30–45.

[28] A. D. Yaghjian. "Approximate formulas for the far field and gain of open-ended rectangular waveguide". *IEEE Trans. Antennas Propag.* 32 (4) (1984): pp. 378–384.

[29] R. Zoughi. "Microwave Non-Destructive Testing and Evaluation Principles". Vol. 4. Springer Science & Business Media, 2012.